

See discussions, stats, and author profiles for this publication at: <https://www.researchgate.net/publication/241552188>

WHAM Observations of H α , [S II], and [N II] toward the Orion and Perseus Arms: Probing the Physical Conditions of the Warm Ionized Medium

Article in The Astrophysical Journal · September 1999

DOI: 10.1086/307734 · Source: arXiv

CITATIONS

221

READS

58

3 authors:



L. Matthew Haffner

University of Wisconsin–Madison

138 PUBLICATIONS 3,295 CITATIONS

SEE PROFILE



Ronald Jay Reynolds

University of Wisconsin–Madison

225 PUBLICATIONS 7,058 CITATIONS

SEE PROFILE



Stephen Tufte

Lewis & Clark College

60 PUBLICATIONS 1,892 CITATIONS

SEE PROFILE

Some of the authors of this publication are also working on these related projects:



A Survey of the Magellanic System with the Wisconsin H-Alpha Mapper [View project](#)

WHAM OBSERVATIONS OF H α , [S II], AND [N II] TOWARD THE ORION AND PERSEUS ARMS: PROBING THE PHYSICAL CONDITIONS OF THE WARM IONIZED MEDIUM

L. M. HAFFNER, R. J. REYNOLDS, AND S. L. TUFTE

Department of Astronomy, University of Wisconsin–Madison, 475 North Charter Street, Madison, WI 53706; haffner@astro.wisc.edu,
 reynolds@astro.wisc.edu, tuft@astro.wisc.edu

Received 1999 March 1; accepted 1999 May 5

ABSTRACT

A large portion of the Galaxy ($l = 123^\circ$ – 164° , $b = -6^\circ$ to -35°), which samples regions of the Local (Orion) spiral arm and the more distant Perseus arm, has been mapped with the Wisconsin H α Mapper (WHAM) in the [S II] $\lambda 6716$ and [N II] $\lambda 6583$ lines. By comparing these data with the maps from the WHAM H α Sky Survey, we begin an investigation of the global physical properties of the warm ionized medium (WIM) in the Galaxy. Several trends noticed in emission-line investigations of diffuse gas in other galaxies are confirmed in the Milky Way and extended to much fainter emission. We find that the [S II]/H α and [N II]/H α ratios increase as absolute H α intensities decrease. For the more distant Perseus arm emission, the increase in these ratios is a strong function of Galactic latitude, b , and thus of height, z , above the Galactic plane, while the [S II]/[N II] ratio is relatively independent of H α intensity. Scatter in this ratio appears to be physically significant, and maps of [S II]/[N II] suggest that regions with similar ratios are spatially correlated. The Perseus arm [S II]/[N II] ratio is systematically lower than local emission by 10%–20%. With [S II]/[N II] fairly constant over a large range of H α intensities, the increase of [S II]/H α and [N II]/H α with $|z|$ seems to reflect an increase in temperature. Such an interpretation allows us to estimate the temperature and ionization conditions in our large sample of observations. We find that WIM temperatures range from 6000 to 10,000 K, with temperature increasing from bright to faint H α emission (low to high [S II]/H α and [N II]/H α), respectively. Changes in [S II]/[N II] appear to reflect changes in the local ionization conditions (i.e., the S^+/S^{++} ratio). We also measure the electron scale height in the Perseus arm to be 1.0 ± 0.1 kpc, confirming earlier, less accurate determinations.

Subject headings: Galaxy: halo — H II regions — ISM: atoms — ISM: structure

1. INTRODUCTION

Although the Wisconsin H α Mapper (WHAM) Sky Survey will present the first view of the distribution and kinematics of the warm ionized medium (WIM), we still know little about the physical conditions in this gas or how they are produced. Several studies have measured constraints on important parameters toward specific regions of the WIM, but none have yet provided a large sample of measurements to help test how environmental conditions (e.g., distance from H II regions, distance from the Galactic plane, and so on) might affect these physical conditions.

Reynolds (1985a) derived the first estimate of the temperature of the WIM by combining measured line widths of [S II] and H α emission toward the same regions. He was able to place limits between 5000 and 20,000 K, with a mean of about 8000 K, on the temperature of a sample of 21 WIM observations. Ionization conditions have been probed even less, with most of our current information coming from observations in the plane of the Galaxy. Reynolds (1985b) showed that [O III] $\lambda 5007$ emission is very faint in the WIM, placing limits on the amount of O^{++} (needing $h\nu > 35.1$ eV) in the WIM. More conclusively, Reynolds & Tuft (1995) and Tuft (1997) have shown via observations of the He I $\lambda 5876$ recombination line that the fraction of He^+ (needing $h\nu > 24.6$ eV) in this gas is also quite low in comparison with traditional O star H II regions. The recent detection of [O I] $\lambda 6300$ from three WIM directions (Reynolds et al. 1998a) places further limits on the ionizing spectrum. The low [O I]/H α ratios seen in all three directions suggest that the H is mostly H^+ in the H α -emitting gas.

The advent of WHAM provides a unique opportunity to trace some of these diagnostics over a larger region of the sky. This paper presents the first velocity-resolved study of [S II] and [N II] from the diffuse gas of our Galaxy. A region of the sky that includes the Perseus arm was chosen for examination since the H α emission from the WIM in this arm is well separated in velocity from local WIM emission and can be traced to high Galactic latitude, allowing an exploration of the emission with distance, z , from the Galactic plane. Such observations can be directly compared with studies of edge-on galaxies, most notably those by Rand (1997, 1998) of NGC 891. The primary trends found in his work are borne out here and extended to even fainter emission measures. Specifically, [S II]/H α and [N II]/H α ratios increase with $|z|$, while [S II]/[N II] ratios remain nearly constant.

A brief description of the instrument and observations are presented in § 2. The results from the data, including a measurement of the electron scale height in the Perseus arm and an investigation of the trends in line ratios, are presented in § 3. In § 4, we present our interpretation that these line ratios provide direct measurements of the temperature and ionization state of the WIM. Finally, our conclusions are summarized in § 5.

2. OBSERVATIONS

2.1. The WHAM Instrument

Because of the extended nature of the WIM, large-aperture Fabry-Perot detection techniques have proven to be quite successful in studying the WIM (Reynolds et al. 1990). For WHAM, a 6 inch (0.15 m), dual-etalon Fabry-

TABLE 1
ATMOSPHERIC LINES IN [S II] AND [N II]
OBSERVATIONS

Line	Mean ^a (km s ⁻¹)	Width (km s ⁻¹)	Intensity ^b (R)
[S II]	+26.8	0	0.06–0.38
	–72.2	10	0.12–0.29
	–113.2	0	0.03–0.14
[N II]	+25	0	0.05–0.10
	–76	10	0.00–0.05
	–40 ^c	0 ^c	0.05–0.10 ^c

^a With respect to the geocentric center of the emission line.

^b Full variation in intensity seen throughout the observation period. Hourly variations are ~ 0.02 R.

^c Contaminated by Perseus arm emission (see text).

Perot spectrometer delivers the high-efficiency, high-resolution observations (Tufté 1997; Reynolds et al. 1998b). The dual-etalon design provides superior order rejection over single-etalon systems to achieve a much larger free spectral range while maintaining high spectral resolution (12 km s⁻¹). An all-sky siderostat housing a 0.6 m lens guides light to the etalon chambers in an environmentally controlled trailer. The center wavelength of the 200 km s⁻¹ spectral window is selected by changing the pressure of a high index of refraction gas (SF₆) in sealed etalon chambers. A narrowband (~ 20 Å FWHM) interference filter provides additional spectral isolation near the desired wavelength. The resulting spectrum, in the form of a Fabry-Perot ring pattern, is imaged onto a cryogenically cooled Tek 1024 × 1024 CCD.

The spectrum covers a 200 km s⁻¹ interval at 12 km s⁻¹ spectral resolution. Coatings on the etalons and optics allow the placement of the 200 km s⁻¹ wide spectral window anywhere between 4800 and 7300 Å. In this “spectral mode,” the image contains only the average spectrum within the 1° diameter circular beam, avoiding confusion between spectral features and angular structures of the source (or stars) within the beam. WHAM also has a set of optics that can be placed in the postetalon beam to provide an extremely narrowband (adjustable between 12 and 200 km s⁻¹), 1' angular resolution *image* of the sky within a 1° field of view. Only the spectral mode (with 1° angular resolution) is used for the observations presented here. Further details on the WHAM spectrometer and its calibration can be found in Tufté (1997).

WHAM is currently located at Kitt Peak National Observatory. Using the WIYN messaging system designed by Percival (1994, 1995) and custom hardware designed by the Space Astronomy Lab at Wisconsin, WHAM is a completely remotely operated telescope system. All functions of the siderostat and spectrometer are routinely operated from our Wisconsin offices. Details on the hardware and software used to operate WHAM and to automate the survey can be found in Haffner (1999).

2.2. The Data

The H α observations of the 1100 deg² region $l = 123^\circ$ – 164° , $b = -6^\circ$ to -35° that is the focus of this study were obtained between 1997 July and October as a part of the WHAM H α Sky Survey (Haffner 1999). Additional observations at the same survey grid points but with the 200 km

s⁻¹ spectral window tuned near the [S II] $\lambda 6716$ and [N II] $\lambda 6583$ lines were obtained in 1997 October, 1997 November, and 1998 June. The region presented here is sampled by 1360 H α , 1360 [S II], and 1360 [N II] spectra, each representing the integrated emission within WHAM's 1° beam. The integration time for each spectrum was 30 s for H α and 60 s for the other two emission lines.

The [S II] and [N II] observations were converted into spectra using the same steps as those for H α presented in Haffner (1999). Separate white-light flat fields were created for each of these additional filters and used in place of the H α flat field. There are no strong terrestrial components in [S II] or [N II] comparable to the geocoronal emission in the H α spectra. For the [S II] observations, the weak terrestrial (Tucson lights) Ne I line at 6717.04 Å was used for velocity calibration. For the [N II] observations, spectra of H α and [N II] from bright emission nebulae were compared, and the velocity frame of [N II] was adjusted so that the mean velocity of the nebular [N II] emission matched that of the H α . By using the terrestrial lines in the H α spectra (geocoronal H α) and [S II] spectra (Ne I), the velocity scale in each spectrum is calibrated to better than 1 km s⁻¹. Intensities were calibrated by applying a correction factor to the [S II] and [N II] observations (0.94 and 1.15, respectively) based on the transmission differences between these filters and the H α filter.

As in the H α observations, the [S II] and [N II] spectra are contaminated by weak atmospheric lines (Haffner, Reynolds, & Tufté 1998; Haffner 1999). The brightest of these in our [S II] spectra is the Ne I line located 26.8 km s⁻¹ from the geocentric zero of [S II] $\lambda 6716$. As noted above, it proves to be a useful wavelength calibrator. To characterize the parameters of these faint lines in the [S II] and [N II] spectra accurately, we followed the same strategy outlined in Haffner (1999) for H α . We first created an average spectrum for each survey “block” (≈ 49 pointings taken sequentially). Using this high signal-to-noise ratio spectra, a single Gaussian was fitted to each of the atmospheric lines and then subtracted from the individual pointings. Such corrections account for hourly variations in these faint lines (typically ~ 0.02 R). A list of the atmospheric lines in our [S II] and [N II] observations is given in Table 1. The potential atmospheric line at -40 km s⁻¹ in [N II] is coincident with interstellar emission from the Perseus arm in all spectra presented here. The implications of such a line are discussed in § 4.

3. RESULTS

3.1. Overview

Figure 1 shows samples of H α , N II, and S II spectra from the region under study. The Local (centered near 0 km s⁻¹) and Perseus arm (centered near -40 to -60 km s⁻¹) emission are shown as well-separated components in the right-hand panels, where $l < 150^\circ$, while local gas dominates in the left-hand panels ($l > 150^\circ$). Figures 2a and 3a display H α intensity maps integrated over $v_{\text{LSR}} = -10$ to $+10$ km s⁻¹ (Fig. 2) and $v_{\text{LSR}} = -30$ to -50 km s⁻¹ (Fig. 3), sampling the Local and Perseus arms, respectively. The boxes overplotted in them denote the $10^\circ \times 12^\circ$ region previously mapped in H α by Reynolds (1980) and compared with H I observations in detail by Reynolds et al. (1995). The [S II] and [N II] maps look qualitatively similar to H α and are not reproduced here. The line ratio images [N II]/H α (Figs.

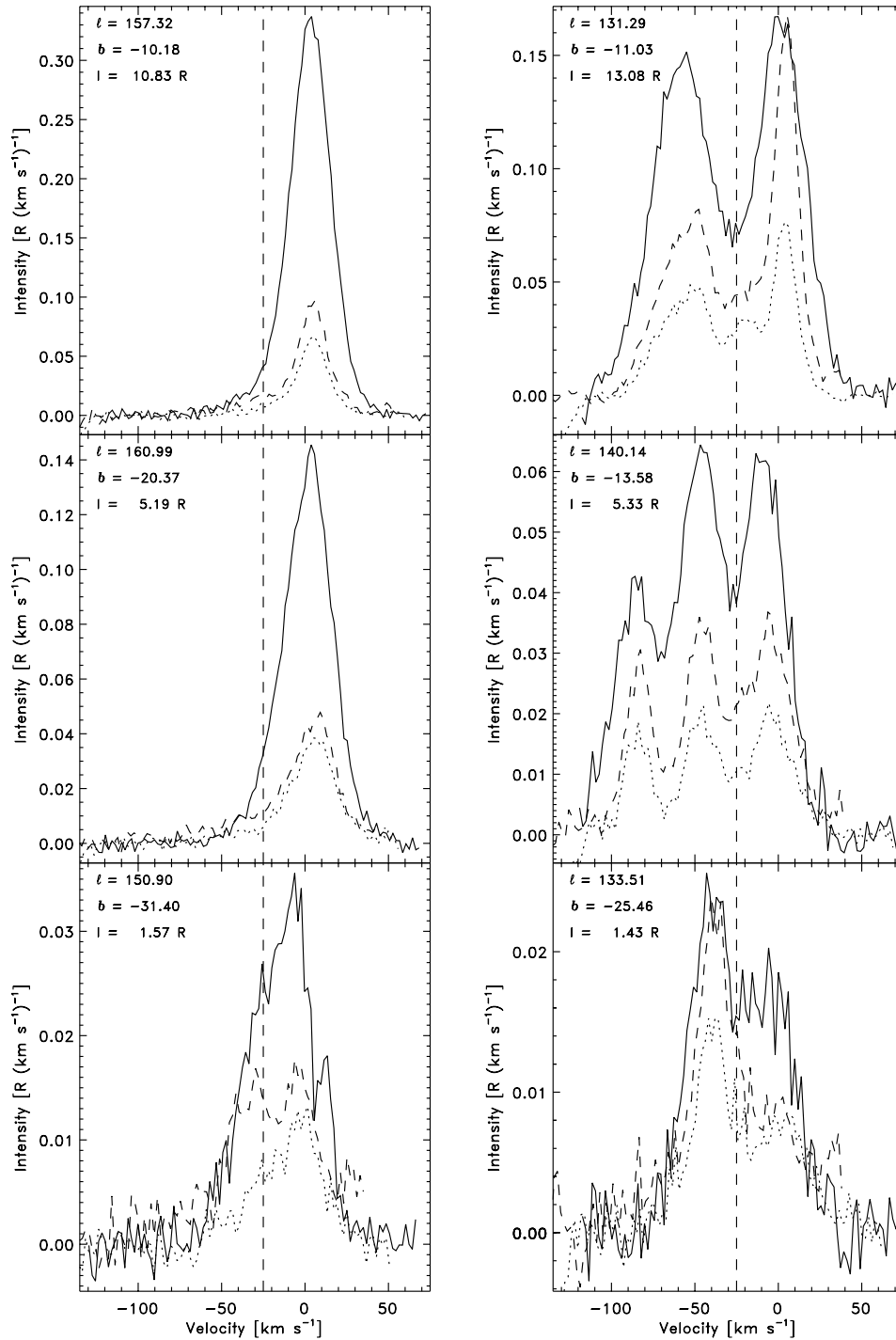


FIG. 1.—Sample H α (solid line), [N II] (dashed line), and [S II] (dotted line) spectra from several directions are plotted as intensity vs. LSR velocity. The total integrated intensity of the emission is labeled in the upper left-hand corner of each plot. The dashed vertical line denotes the delineation for integration ranges between the Local and Perseus arms in this paper.

2b and 3b), [S II]/H α (Figs. 2c and 3c), and [S II]/[N II] (Figs. 2d and 3d) are discussed in § 3.3.

Two large H α -emitting regions dominate the emission at lower latitudes, above $b = -20^\circ$. The brightest emission arises from NGC 1499 (California Nebula) excited by the O7.5 I star ξ Per located 540^{+330}_{-150} pc away (*Hipparcos*; ESA 1997) at $l = 160^\circ 37'$, $b = -13^\circ 11'$. Emission in the nebula itself, a $5^\circ \times 2^\circ$ crescent centered near $l = 160^\circ$, $b = -13^\circ$, peaks at over 250 R (1 R = $10^6/4\pi$ photons cm⁻² s⁻¹ sr⁻¹ = 2.4×10^{-7} ergs cm⁻² s⁻¹ sr⁻¹ at H α) and is cen-

tered around $v_{\text{LSR}} = -5$ km s⁻¹, while faint, extended emission above 5 R centered near $v_{\text{LSR}} = +5$ km s⁻¹ continues 5° – 7° away from the nebula. This extended H II region has been studied in some detail by Reynolds (1988), who first hypothesized that the bar of emission ($I_{\text{H}\alpha} \approx 8$ R) running from $l = 150^\circ$, $b = -20^\circ$ to $l = 142^\circ$, $b = -10^\circ$ centered between $v_{\text{LSR}} = -5$ and $+5$ km s⁻¹ may also be ionized by the star.

The second large emission region, centered near $l = 131^\circ$, $b = -11^\circ$, is a superposition of separate but equally bright

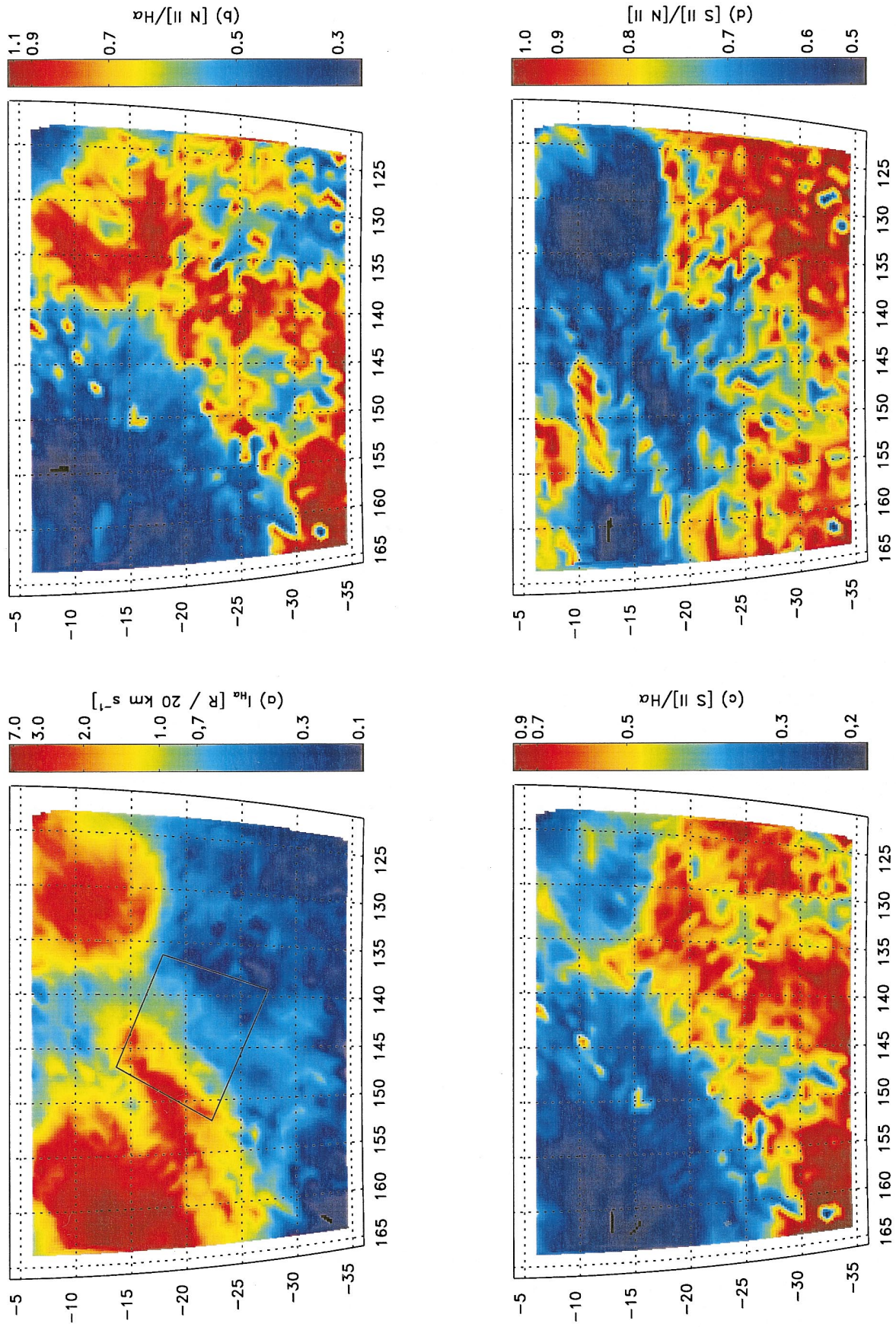


FIG. 2.—(a) H α emission from the local Orion arm. This pseudocolor image shows the H α emission integrated over $v_{\text{LSR}} = -10$ to $+10 \text{ km s}^{-1}$. The axes are Galactic longitude and latitude. The overlaid box shows the location of the original H α background survey in this region (see text). Emission-line ratio maps of (b) $[\text{N II}]/\text{H}\alpha$, (c) $[\text{S II}]/\text{H}\alpha$, and (d) $[\text{S II}]/[\text{N II}]$ are also shown for the same velocity band. The color scale in each image is histogram-equalized to enhance spatial detail.

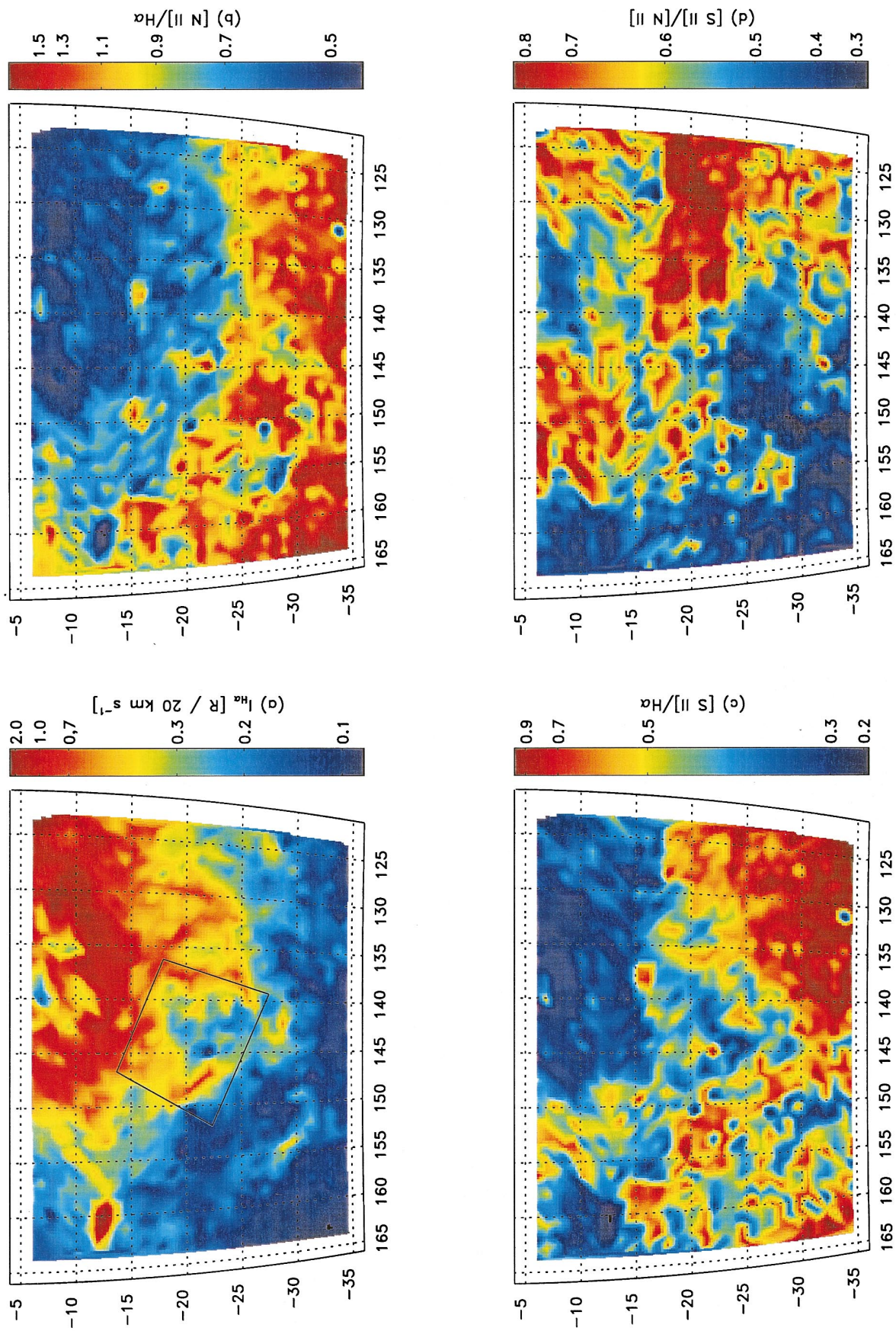


FIG. 3.—(a) H α emission from the Perseus arm, approximately 2.5 kpc distant. This pseudocolor image shows the H α emission integrated over $v_{\text{LSR}} = -50$ to -30 km s^{-1} . The axes are Galactic longitude and latitude. The overlaid box shows the location of the original H α background survey in this region (see text). Emission-line ratio maps of (b) $[N \text{ II}]/H\alpha$, (c) $[S \text{ II}]/H\alpha$, and (d) $[S \text{ II}]/[N \text{ III}]$ are also shown for the same velocity band. The color scale in each image is histogram-equalized to enhance spatial detail.

emission regions in the Local and Perseus arms (see Fig. 1). Emission from the Local arm is near $v_{\text{LSR}} = 0 \text{ km s}^{-1}$ and has a more circular appearance reminiscent of a classical Strömgren sphere (see Fig. 2a). This faint H II region has a relatively constant brightness of 5–6 R over most of its 13° diameter area. The most promising candidate for an ionizing source for this region is ϕ Per, a B0.5e+sdO binary system located at $l = 131.3$, $b = -11.3$ and 220^{+43}_{-32} pc away (*Hipparcos*; ESA 1997; Gies et al. 1998). At that distance, the region is 50 pc in diameter. Some details of this region can be found in Haffner (1999). A future study (Haffner et al. 1999) examining the properties of B-star H II regions in the WHAM H α Sky Survey will expand on this work. Emission from the Perseus arm in this direction at $-60 < v_{\text{LSR}} < -40$ is much more amorphous in shape (Fig. 3a).

At higher latitudes and at velocities farther from the LSR, the H α emission becomes quite filamentary. Some of the more notable structures include a faint bar in Figure 3a running from $l = 150^\circ$, $b = -33^\circ$ to $l = 160^\circ$, $b = -25^\circ$; several, nearly vertical filaments near $l = 130^\circ$, $b = -20^\circ$; and the shell-like region and associated dissecting filament (more visible at higher velocities; see Haffner 1999) centered on the box in Figure 3a. The last of these was previously studied in detail by Ogden & Reynolds (1985) and Reynolds et al. (1995).

3.2. Scale Height of the WIM

Since the Perseus arm gas is well separated in velocity from the local emission, we can explore the decrease of this emission as a function of the height above the Galactic plane. To extract information about the scale height from the intensity distribution, we first assume that the gas density is primarily a function of z and has the form

$$n_e(z) = n_e^0 e^{-|z|/H} \text{ cm}^{-3}, \quad (1)$$

where n_e^0 is the midplane density and H is the scale height of the WIM. The H α intensity is related to the gas density by the equation

$$2.75 T_4^{0.9} I_{\text{H}\alpha} = \int \phi n_e^2 dl, \quad (2)$$

where ϕ is the filling fraction of the emitting gas, T_4 is the temperature of the gas in 10^4 K , and $I_{\text{H}\alpha}$ is in rayleighs. As long as the temperature, filling factor, and path length through the emitting gas, $\int dl = L$, are not functions of z , we then have

$$I_{\text{H}\alpha} = \frac{\phi(n_e^0)^2 L}{2.75 T_4^{0.9}} e^{-2|z|/H} = I_{\text{H}\alpha}^0 e^{-2|z|/H}, \quad (3)$$

where $I_{\text{H}\alpha}^0$ is the intensity at the midplane. Finally, substituting $z = D \tan |b|$, where D is the distance to the arm and b is the Galactic latitude of an observation, and taking the natural log, we arrive at

$$\ln I_{\text{H}\alpha} = \ln I_{\text{H}\alpha}^0 - \frac{2D}{H} \tan |b|. \quad (4)$$

Figure 4 plots this relationship for a selected region of the map. Each point represents the median emission between $l = 125^\circ$ and 152° for each Galactic latitude. The median of the emission in each latitude slice is used instead of an average to reduce the effect of local emission enhancements

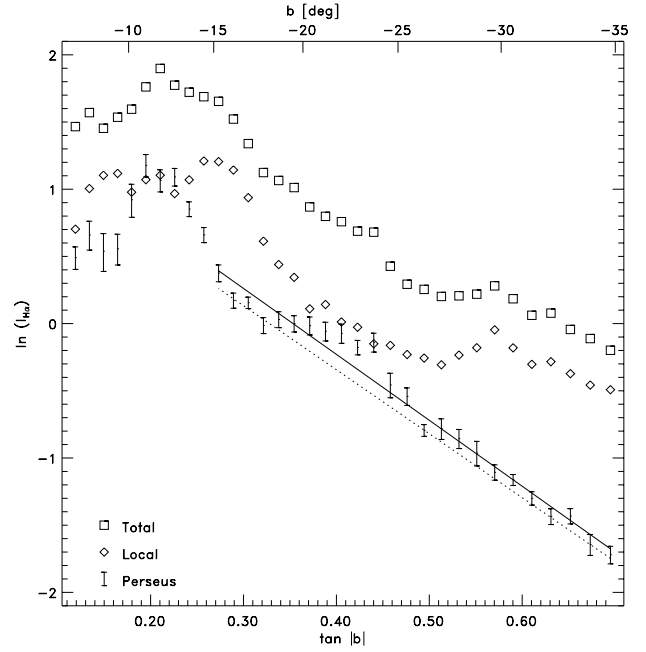


FIG. 4.—Natural logarithm of the median H α intensity between $l = 125^\circ$ and 152° plotted vs. the tangent of Galactic latitude. Total ($v_{\text{LSR}} = -100$ to $+100 \text{ km s}^{-1}$), Local ($v_{\text{LSR}} = -25$ to $+100 \text{ km s}^{-1}$), and Perseus arm ($v_{\text{LSR}} = -100$ to -25 km s^{-1}) emission are denoted by squares, diamonds, and vertical bars, respectively. A linear best fit to the Perseus arm emission above $b = -15^\circ$ is displayed as a solid line. The dotted line is a fit to the lower envelope of the data (see § 3.2).

(e.g., faint H II regions). The limited longitude range is chosen to avoid the gradual blending of the Perseus arm component with the local gas as the longitude approaches 180° . Three radial velocity intervals are presented in the plot, reflecting total ($v_{\text{LSR}} = -100$ to $+100 \text{ km s}^{-1}$), Local ($v_{\text{LSR}} = -25$ to $+100 \text{ km s}^{-1}$), and Perseus arm ($v_{\text{LSR}} = -100$ to -25 km s^{-1}) emission. The integration ranges are expanded from the limited ranges in Figures 2 and 3 to include the full emission profile in our calculations. The error bars for the Perseus arm are an estimate of the physical scatter along a latitude slice calculated from the average deviation about the median of emission within that slice.

Also displayed in Figure 4 is a linear fit to Perseus arm points that are above $b = -15^\circ$. Closer to the plane, H II regions and extinction play a significant role, and these points are excluded from the fit. The resulting fit parameters are $\ln I_{\text{H}\alpha}^0 = 1.73 \pm 0.19$ and $2D/H = 4.91 \pm 0.39$, leading to a midplane intensity for the WIM of $5.7 \pm 0.2 \text{ R}$ and a scale height of $1.0 \pm 0.1 \text{ kpc}$ if the Perseus arm is at $D = 2.5 \text{ kpc}$ (see Reynolds et al. 1995 and references therein). The dotted line in Figure 4 presents a manual fit to the lower envelope of the Perseus arm emission. The resulting parameters are essentially the same: $H = 1.0 \text{ kpc}$ and $I_{\text{H}\alpha}^0 = 4.2 \text{ R}$. The 1.0 kpc scale height appears to be valid for $|z|$ from 750 pc to at least 1700 pc , the boundary of this studied region.

As mentioned above, this estimate assumes that the filling fraction and temperature do not depend on $|z|$. If in fact ϕ changes as a function of height above the plane, it affects our estimate of the electron scale height. As shown in § 4, these new observations suggest that the temperature in the WIM rises with distance from the Galactic plane. Such an effect would increase our estimate of the scale height.

Finally, we also note here that the full role of interstellar extinction has not been taken into account within our restricted fitting region. Future observations of $H\beta$ will allow a straightforward correction of the $H\alpha$ data for this attenuation. A simplistic estimate of the magnitude of this correction within our fitted region suggests a decrease in the inferred scale height of $\sim 10\%$, somewhat offsetting the expected effect of $T(|z|)$.

3.3. Line Ratios

Figures 2 and 3 also present pseudocolor images of (b) $[N II]/H\alpha$, (c) $[S II]/H\alpha$, and (d) $[S II]/[N II]$ line ratios integrated over $v_{LSR} = -10$ to $+10$ km s^{-1} (Fig. 2) and $v_{LSR} = -30$ to -50 km s^{-1} (Fig. 3), sampling the Local and Perseus arms, respectively. The $[N II]/H\alpha$ and $[S II]/H\alpha$ maps in both arms generally anticorrelate with $H\alpha$ emission, except for the ϕ Per $H II$ region centered near $l = 131^\circ$, $b = -11^\circ$ mentioned in § 3.1. The $[S II]/[N II]$ ratios are generally lower in the two brighter $H II$ regions in the Local arm but otherwise show little additional correspondence to $H\alpha$ maps.

In Figures 5 and 6, $[S II]/H\alpha$ and $[N II]/H\alpha$ are plotted against $H\alpha$ intensity. The radial velocity ranges for each panel of the figures are restricted to separate the Local and

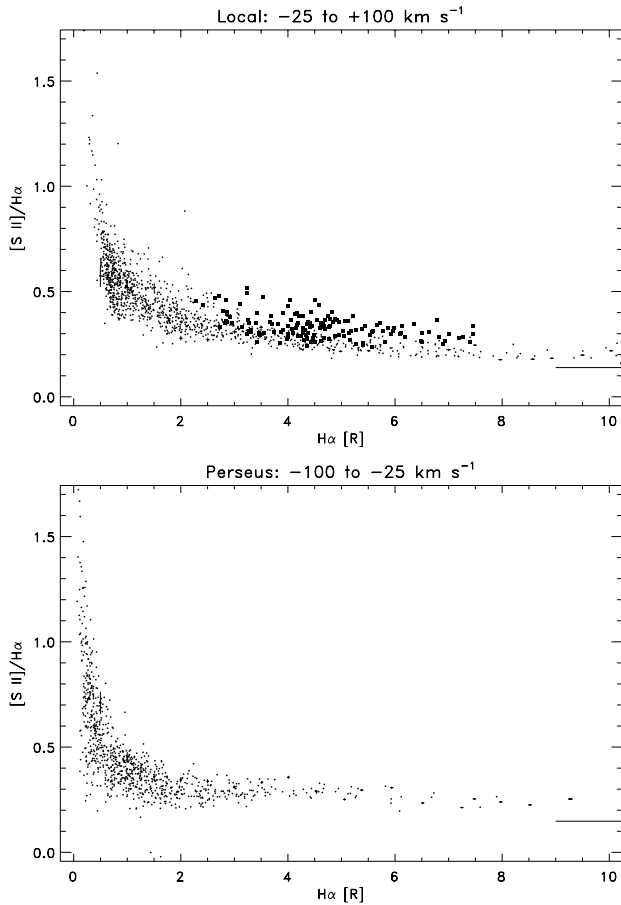


FIG. 5.— $[S II]/H\alpha$ plotted vs. $H\alpha$ intensity for both the Local and Perseus arm emission. For the Perseus arm, the longitude range has been restricted to $l = 125^\circ$ – 152° . Crosses show representative error bars for select points. The uncertainty in the ratio at 0.5 R is 7%–8%. Filled squares denote pointings within 6.5 of the center of the ϕ Per $H II$ region mentioned in § 3.1: $l = 131^\circ$, $b = -11^\circ$. The solid line denotes the average ratio of pointings with $I_{H\alpha} > 50$ R (i.e., “classical” $H II$ regions).

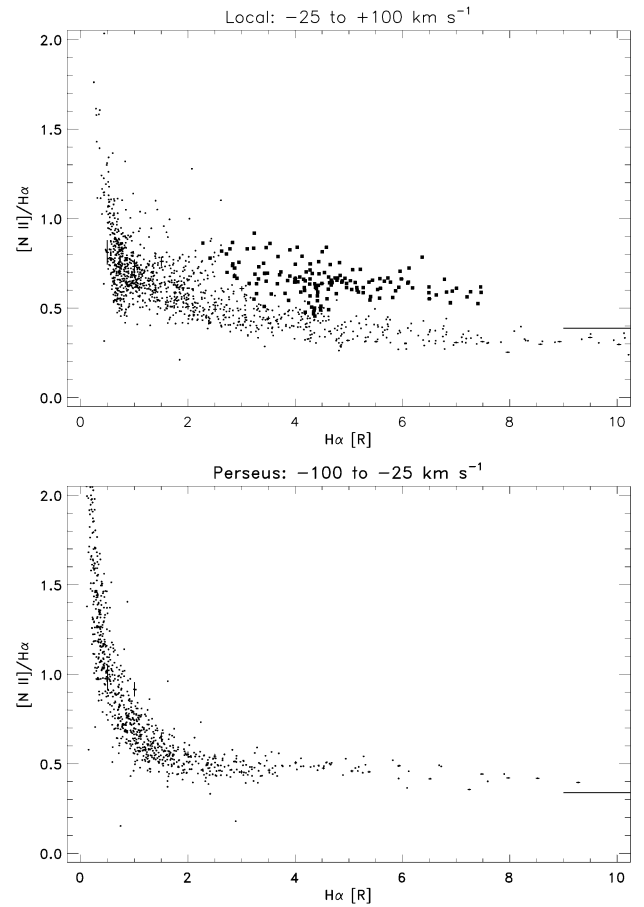


FIG. 6.—Same as Fig. 5, but for $[N II]/H\alpha$ vs. $H\alpha$

Perseus arm emission (see Fig. 1). As above, the longitudinal extent of the Perseus observations is limited to $l < 152^\circ$. We denote the pointings within the newly discovered ϕ Per $H II$ region (see § 3.1) with a square. Note that these points appear to form the upper envelope of the $[S II]/H\alpha$ ratios for their $H\alpha$ intensities (Fig. 5) and actually form a distinctly different horizontal branch in the $[N II]/H\alpha$ ratios (Fig. 6). In general, both figures show a marked increase in these ratios with decreasing $H\alpha$ intensity. For comparison with a more traditional $H II$ region in this mapped area, the horizontal solid line at the right edge of both figures shows the average ratio from the six pointings with $I_{H\alpha} > 50$ R near NGC 1499: $[S II]/H\alpha = 0.14$ and $[N II]/H\alpha = 0.39$. Ratios for a brighter $H II$ region, our calibration source NGC 7000 ($I_{H\alpha} = 800$ R), are $[S II]/H\alpha = 0.06$ and $[N II]/H\alpha = 0.20$ (see also Reynolds 1985a).

Figure 7 plots these two line ratios against one another. In both the Local and Perseus arms, the ratios appear to be strongly correlated. In this figure, the ϕ Per (B-star) and ξ Per (O-star) $H II$ regions are highlighted with squares and triangles, respectively. Both appear to occupy specific loci that are different not only from one another, but from the general WIM background. The Perseus arm panel is again restricted to $l < 152^\circ$.

As discussed in § 3.2, the general trend in $H\alpha$ intensity is that it decreases as the observed gas lies farther from the Galactic plane. Figure 8 shows that the relationship of the $[S II]/H\alpha$ and $[N II]/H\alpha$ ratios versus $H\alpha$ intensity described above translates directly into an increase of these ratios

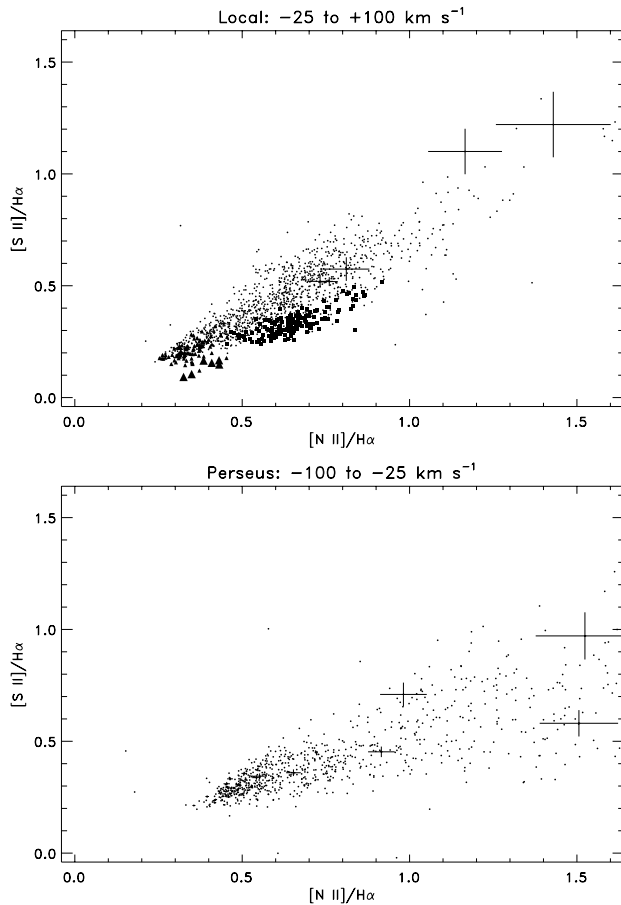


FIG. 7.—Same as Fig. 6, but for $[S II]/H\alpha$ vs. $[N II]/H\alpha$. Additional plot symbols (triangles) denote pointings within 5° of the (rough) center of the ξ Per H II region: $l = 160^\circ$, $b = -15^\circ$.

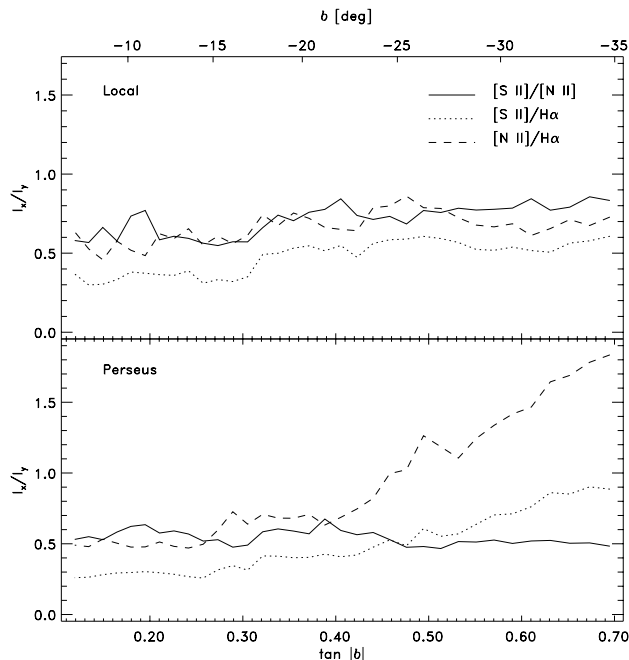


FIG. 8.—Three emission-line ratios vs. the tangent of Galactic latitude: $[S II]/H\alpha$ (dotted line), $[N II]/H\alpha$ (dashed line), and $[S II]/[N II]$ (solid line). Each data point represents the ratio of the median emission between $l = 125^\circ$ and 152° . Intensities have been integrated over the velocity range $v_{LSR} = -25$ to 100 km s $^{-1}$ for the top panel and $v_{LSR} = -100$ to -25 km s $^{-1}$ in the bottom panel.

with increasing $|b|$ (or $|z|$) in the Perseus arm. The figure shows the three line ratios $[S II]/H\alpha$, $[N II]/H\alpha$, and $[S II]/[N II]$ as a function of $\tan |b|$. Both panels are restricted to the longitude range $l = 125^\circ$ – 152° for consistency. Note also that the $[S II]/[N II]$ ratio is relatively constant, with perhaps a slight increase in the Local arm with increasing $|b|$.

4. DISCUSSION

The tight correlation of $[S II]$ and $[N II]$ emission in Figure 7 results in a fairly constant value of $[S II]/[N II]$ over a wide variety of $H\alpha$ intensities and latitudes in both arms. This result has been seen in numerous studies of the extragalactic WIM analogue, commonly referred to as the diffuse ionized gas (DIG; Otte & Dettmar 1999; Rand 1998; Wang, Heckman, & Lehnert 1997; Greenawalt, Walterbos, & Braun 1997). As Rand covers in detail, current photoionization models in which variations in $[S II]/H\alpha$ and $[N II]/H\alpha$ arise primarily from variations in the ionization parameter (e.g., Domgörgen & Mathis 1994; Sokolowski 1994; see also Bland-Hawthorn, Freeman, & Quinn 1997) have difficulty keeping this ratio constant as $[S II]/H\alpha$ and $[N II]/H\alpha$ rise. Abundance gradients and H II region contamination can be a larger problem in interpreting such ratios in extragalactic studies with the large physical sizes represented by a typical data point. Our new observations within the Galaxy provide smaller scales and adequate velocity resolution to separate radial components of gas, avoiding some of these problems.

We suggest that the tight correlation of $[S II]/[N II]$ seen in our data arises simply from the dominance of S^+ and N^+ ionization states in this gas together with the similar excitation potential of these two emission lines. With increasing electron temperature, $[S II]/H\alpha$ and $[N II]/H\alpha$ ratios rise together with no change in the $[S II]/[N II]$ ratio. Using this premise, namely, that variations in these ratios are due primarily to variations in electron temperature, we attempt to derive estimates of the electron temperature and ionization state of S within our sample. We start with the basic equation for the intensity of emission lines from collisionally excited ions,

$$I_\nu (\text{photons s}^{-1} \text{ cm}^{-2} \text{ sr}^{-1}) = \frac{f_\nu}{4\pi} \int n_i n_e \frac{8.63 \times 10^{-6}}{T^{0.5}} \frac{\Omega(i, j)}{\omega_i} e^{-(E_{ij}/kT)} dl \quad (5)$$

(Osterbrock 1989), where $\Omega(i, j)$ is the collision strength of the transition, ω_i is the statistical weight of the ground level, E_{ij} is the energy of the upper level of the transition above the lower, and f_ν is the fraction of downward transitions that produce the emission line in question. We adopt the following parameterized representations of the collision strengths supplied by Aller (1984), valid from 5000 to 20,000 K:

$$S^+ : \Omega(4S_{3/2}, 2D_{5/2}) = 4.19 T_4^{-0.093}, \quad (6)$$

$$N^+ : \Omega(3P, 1D) = 2.68 T_4^{0.026}, \quad (7)$$

where T_4 is in units of 10^4 K. A term to account for extinction has not been included in equation (5), since the three lines we are comparing are close in wavelength.

To arrive at any estimates, we must be able to compute the path-averaged integrals in these equations. Since there is little knowledge yet of the details of the spatial distribution

of the physical parameters in the WIM, we take the simplest approach and assume that physical values do not vary along a path. For the ratios we calculate below, we need to make this assumption for the temperature, ionization, and abundance of the gas. Our estimates should then be viewed as representative values, rather than as accurately reflecting local conditions from where the emission arises. Since we are able to separate Local and Perseus arm gas cleanly, large-scale Galactic variations can be probed along lines of sight, even with this assumption. This simplification also implies that the line emission from the three ions originates from the same location. This is probably a valid assumption in the WIM, unless local processes on small scales (e.g., shocks) dominate the ionization structure. In the brighter, discrete H II regions, however, this assumption most likely breaks down since the ionization structure of the nebula could be changing significantly within our beam.

With this simplification, we arrive at these two equations for the intensity of [S II] and [N II] emission:

$$I_{6716}(R) = 2.79 \times 10^5 \left(\frac{H^+}{H} \right)^{-1} \left(\frac{S}{H} \right) \times \left(\frac{S^+}{S} \right) T_4^{-0.593} e^{-2.14/T_4} \text{ EM}, \quad (8)$$

and

$$I_{6583}(R) = 5.95 \times 10^4 \left(\frac{H^+}{H} \right)^{-1} \left(\frac{N}{H} \right) \times \left(\frac{N^+}{N} \right) T_4^{-0.474} e^{-2.18/T_4} \text{ EM}, \quad (9)$$

where T_4 is in units of 10^4 K and $\text{EM} = \int n_e^2 dl$ is the emission measure in units of cm^{-6} pc. Note also that I is now in units of rayleighs. The [S II]/[N II] intensity ratio is then

$$\frac{I_{6716}}{I_{6583}} = 4.69 \frac{(S/H)}{(N/H)} \frac{(S^+/S)}{(N^+/N)} e^{0.04/T_4} T_4^{-0.119}. \quad (10)$$

We use the solar $(S/H) = 1.86 \times 10^{-5}$ from Anders & Grevesse (1989) and $(N/H) = 7.5 \times 10^{-5}$ from Meyer, Cardelli, & Sofia (1997) for the gas-phase abundances of S and N.

Because of the similar first ionization potentials of N and H (14.5 and 13.6 eV) and a weak charge-exchange reaction, N^+/N^0 tracks H^+/H^0 in photoionization models (Sokolowski 1994), so that in H α -emitting regions, where the fractional ionization of H has been measured to be near unity (Reynolds et al. 1998a), $N^+/N \rightarrow 1$ also. However, with a second ionization potential of 29.6 eV, N most likely ionizes no higher than N^+ . Recent photoionization models run by Howk & Savage (1999) over a wide range of temperatures and ionization parameters show that even if the ionizing spectrum in the WIM is as hard as $T_e \approx 40,000$ K, $N^{++}/N < 0.3$. Furthermore, Reynolds & Tufté (1995) and Tufté (1997) found that He^+/He ranges from 0.3 to about 0.6 in the WIM, suggesting a spectrum that is significantly softer than 40,000 K and therefore implying a very small N^{++}/N ratio. Sulfur, on the other hand, has a low enough first ionization potential, 10.4 eV, that it is most likely fully ionized in the gas we are studying. In addition, its second potential, 23.4 eV, lies slightly below the neutral He edge at 24.6 eV. The existence of He^+ in the WIM (Reynolds &

Tufté 1995; Tufté 1997) and the model calculations of Howk & Savage (1999) both imply that, indeed, some S will be ionized to S^{++} .

In the limit where S^+/S and N^+/N are both unity and at a typical WIM temperature of $T_4 = 0.8$, equation (10) gives $I_{6716}/I_{6583} = 1.26$. This relationship is plotted as the solid line in Figure 9. Dotted lines of lower slope show the effect of decreasing S^+/S (presumably due to an increase in S^{++}) while keeping $N^+/N = 1$. In this interpretation, the data imply that S^+/S ranges between about 0.25 and 0.8, with an average value for the local diffuse background of 0.6–0.65. Note that the location of the H II region symbols (*filled triangles and squares*) in Figure 9 indicate that these regions have systematically lower S^+/S than the diffuse background. In these cases, the lower ratios are more likely due to the expected behavior that closer to the ionizing source, where the ionization parameter is large, more S^+ is ionized to S^{++} , producing a corresponding decrease in the observed [S II] intensity relative to H α (Domgörgen & Mathis 1994; Sokolowski 1994).

Just as the [N II]/H α and [S II]/H α ratios together can give us information on the ionization state of S, examining the ratios alone can provide some estimate of the temperature. From equations (2) and (9), the [N II]/H α ratio is given by

$$\frac{I_{6583}}{I_{\text{H}\alpha}} = 1.63 \times 10^5 \left(\frac{H^+}{H} \right)^{-1} \left(\frac{N}{H} \right) \left(\frac{N^+}{N} \right) T_4^{0.426} e^{-2.18/T_4}. \quad (11)$$

Since $N^+/N \approx H^+/H$ (see above), the H and N ionization factors can be removed from equation (11), with the result that for a given (N/H) abundance, [N II]/H α is only a function of the electron temperature. As an example, the typical WIM temperature of $T_4 = 0.8$ then leads to [N II]/H $\alpha = 0.72$. Lines of constant temperature are plotted on Figure 9 as dashed vertical lines. With a better estimate for tem-

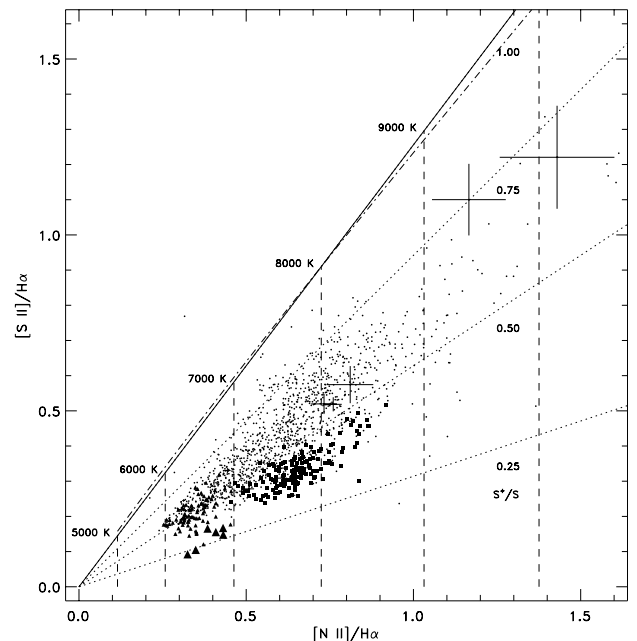


FIG. 9.—Same as Fig. 7 for the Local arm only, except with a grid for inferred temperatures and S^+/S ratios.

perature from this line ratio, we also recompute equation (10), including the temperature dependencies this time, to form the dash-dotted line in Figure 9. This correction is small.

Figure 10 shows the same grid of S^+/S and T overplotted on the Perseus arm ratios. The limits placed on S^{++}/S in the WIM by Howk & Savage (1999) are at odds with the significant number of points below the $S^+/S = 0.5$ line in the Perseus arm. As noted in § 2, there may be an atmospheric line within the integration range of Perseus arm $[N\ II]$ emission. By comparing $[S\ II]$ and $[N\ II]$ spectra toward the same locations, we derive an upper limit of 0.1 R for the intensity of this line. The maximum effect of removing this line is displayed for a few sample points in Figure 10 by translating the solid sample error bar points to the location of the dotted error bars. Such a correction would imply a slightly higher S^+/S ratio on average for the Perseus arm, but not enough to explain the entire difference between the arms. We may be probing a harder radiation field in the Perseus arm gas than their model input spectra, or our assumed value of S/H may be too high. A reduction in the gas-phase sulfur abundance of 0.5–0.75 (0.3–0.1 dex) would bring our inferred S^{++}/S fractions more in line with their models.

The Perseus arm gas appears to have systematically lower S^+/S than the Local arm, with an average value closer to 0.5. Equation (10) shows that differences in abundances between the Local and Perseus arms could change the slope of the $[S\ II]/H\alpha$ and $[N\ II]/H\alpha$ relationship. However, Afflerbach, Churchwell, & Werner (1997) measured the Galactic abundance gradients in ultracompact H II regions for O, S, and N. Using their best fits, N/H falls off faster than S/H with increasing Galactocentric distance so that S/N is $\sim 5\%$ higher in the Perseus arm. This is the opposite effect needed to explain the difference in the

Perseus and Local arm emission ratios. More likely, Figure 10 suggests that this region of the Perseus arm has a higher fraction of S^{++} than the Local arm region. Rand (1998) observed an increase in $[O\ III]/H\beta$ with height above the plane of NGC 891 and concluded that an additional source of ionization is needed beyond photoionization from hot stars in the disk. In a region where O^{++} ions are being maintained, S^+ becomes a less dominant species. This is consistent with the inferred differences in S^+/S between the Perseus arm (Fig. 10) and Local arm (Fig. 9) data, since lines of sight pass through the Perseus arm at much higher $|z|$ than for local gas. One problem with this interpretation is that we do not see a substantial fall in the $[S\ II]/[N\ II]$ ratio with increasing $|z|$ in the Perseus arm (Fig. 8). Instead of an additional ionizing source, it is also possible that there are marked differences in the strength of the halo ionizing field between the Local and Perseus arms. For example, NGC 891 shows considerable variation in the extent of extended $H\alpha$ emission along the Galactic plane (Rand, Kulkarni, & Hester 1990; Rand 1998).

The scatter of data points suggests significant variations in the electron temperature within the mapped region, from about 6000 to 10,000 K. The most striking result from these temperature estimates comes when reexamining the trend of the $[N\ II]/H\alpha$ ratio in Figures 3b and 8. From the rise in this ratio with increasing $|z|$ and equation (11) (or the grid of Fig. 10), we infer that the temperature in the halo rises from about 7000 K at $|z| = 0.75$ kpc ($b \sim -17^\circ$) to over 10,000 K at $|z| = 1.75$ kpc ($b \sim -35^\circ$). If the electron temperature is truly rising with $|z|$ as our results suggest, the calculation of the scale height of $H\alpha$ -emitting gas (§ 3.2) becomes more complicated. If we confirm this effect with future observations (see § 5), the net effect (eq. [2]) is that the true scale height of the gas is larger than the value calculated in § 3.2 by about 20%.

Note also that since fainter regions tend to have higher $[N\ II]/H\alpha$ (Fig. 6), our analysis implies that fainter regions are hotter. Since $EM \propto I_{H\alpha} T^{0.9}$, higher temperature regions naturally produce lower $H\alpha$ intensities for a given EM; however, even after converting $I_{H\alpha}$ to EM using a varying temperature estimate from the $[N\ II]/H\alpha$ observations, regions with lower EM are still hotter. Since EM depends on ϕn_e^2 and the path length through the emitting region, one of the two must be smaller in these fainter, hotter regions. Path length is an inherently unphysical parameter to link to temperature, and we can think of no reason why our data set would bias shorter path length sight lines toward higher temperature regions. Thus we conclude that the hotter regions most likely have smaller $\langle n_e^2 \rangle$. Since n_e in our mapped region of the Perseus arm decreases with increasing $|z|$ (see § 3.2), we are not able to ascertain from these data whether n_e or $|z|$ is the fundamental parameter influencing the electron temperature.

One possible explanation for the discrepancy between these results and photoionization models (e.g., Domgörgen & Mathis 1994; Sokolowski 1994) is that at high $|z|$ or low n_e , an additional heating source may dominate over the heating from photoionization (Bland-Hawthorn et al. 1997). Since the heating per volume from photoionization is proportional to n_e^2 (it is limited by recombination), a heating term that is proportional to n_e or that did not depend on n_e at all would become dominant at sufficiently low densities. Such an effect would decouple the heating from the ionization of atoms, keeping $[S\ II]/[N\ II]$ constant, while driving

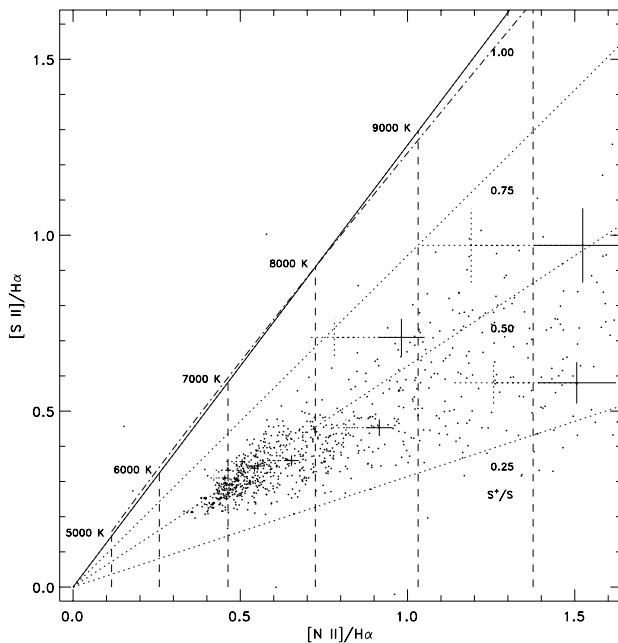


FIG. 10.—Same as Fig. 7 for the Perseus arm only, except with a grid for inferred temperatures and S^+/S ratios. As before, solid crosses denote error bars for representative samples; dotted crosses show how the positioning of these data points would change if a weak terrestrial line at the velocity of the Perseus arm is as bright as 0.1 R (see text).

up the [S II] and [N II] intensities relative to H α . We also note that if such a process exists in the halo, the increase in [O III]/H β seen by Rand (1998) in the halo of NGC 891 could be a direct consequence of this additional heating source and would not require a secondary ionization source. Possible heating sources include, for example, the dissipation of interstellar turbulence (Minter & Spangler 1992) and the photoionization of interstellar grains (Reynolds & Cox 1992). The idea of an additional heating source will be explored further in a related work (Reynolds, Haffner, & Tufte 1999).

5. SUMMARY

We have presented the first comprehensive, velocity-resolved maps of [N II] and [S II] in the Galaxy. Combining the H α maps from the WHAM H α Sky Survey in this region, we draw the following conclusions:

1. We confirm earlier estimates of the distribution of H α emission in the Perseus arm (Reynolds 1997). With continuous coverage from $b = -6^\circ$ to -35° ($|z| = 300\text{--}1750$ pc at $d = 2.5$ pc), we find that the electron distribution derived from the emission is described well by an exponential with a scale height of $H = 1.0 \pm 0.1$ kpc.

2. The [S II]/H α and [N II]/H α emission in our Galaxy shows the same rise with increasing $|z|$ as found in observations of edge-on galaxies (Rand 1998; Golla, Dettmar, & Domgörgen 1996). These ratios appear to be correlated with each other over a wide range of emission measures and $|z|$.

3. We suggest that the correlation between [N II]/H α and [S II]/H α can be attributed to the fact that changes in these ratios are primarily due to changes in electron temperature rather than ionization parameter and that scatter in the relationship is caused by variations in S^+/S . The maps of [N II]/H α and [S II]/[N II] (Figs. 2 and 3) can then be viewed as distributions of electron temperature and ionization state, respectively. With this interpretation, we derive temperatures in the WIM of 6000–10,000 K and S^+/S ratios of 0.3–0.8. The average value of S^+/S appears to be lower in the Perseus arm. Higher ionization and lower temperatures are mostly found in the two H II regions surrounding the O star ξ Per and the B-star system ϕ Per. Differences in temperature between regions may be able to be directly confirmed with observations of the faint, higher level [N II] $\lambda 5755$ transition, which when combined with our $\lambda 6483$ measurements can directly measure the electron temperatures in the emitting gas.

We thank Kurt Jaehnig and Jeff Percival of the University of Wisconsin's Space Astronomy Lab for their dedicated engineering support of WHAM; Nikki Hausen, Mark Quigley, and Brian Babler for their contributions to the data analysis; and Trudy Tilleman for essential night-sky condition reports from Kitt Peak, which have made remote observing possible. We acknowledge the use of the SIMBAD database, operated at CDS, Strasbourg, France. This work is supported by the National Science Foundation through grant AST 96-19424.

REFERENCES

- Afflerbach, A., Churchwell, E., & Werner, M. W. 1997, *ApJ*, 478, 190
 Aller, L. H. 1984, *Physics of Thermal Gaseous Nebulae* (Dordrecht: Reidel)
 Anders, E., & Grevesse, N. 1989, *Geochim. Cosmochim. Acta*, 53, 197
 Bland-Hawthorn, J., Freeman, K. C., & Quinn, P. J. 1997, *ApJ*, 490, 143
 Domgörgen, H., & Mathis, J. S. 1994, *ApJ*, 428, 647
 ESA. 1997, *The Hipparcos and Tycho Catalogues*, ed. M. A. C. Perryman (ESA SP-1200; Noordwijk: ESA/ESTEC)
 Gies, D. R., Bagnuolo, W. G., Jr., Ferrara, E. C., Kaye, A. B., Thaller, M. L., Penny, L. R., & Peters, G. J. 1998, *ApJ*, 493, 440
 Golla, G., Dettmar, R.-J., & Domgörgen, H. 1996, *A&A*, 313, 439
 Greenawalt, B., Walterbos, R. A. M., & Braun, R. 1997, *ApJ*, 483, 666
 Haffner, L. M. 1999, Ph.D. thesis, Univ. Wisconsin–Madison
 Haffner, L. M., Reynolds, R. J., & Tufte, S. L. 1998, *ApJ*, 501, L83
 ———. 1999, in preparation
 Howk, J. C., & Savage, B. D. 1999, *ApJ*, 517, 746
 Meyer, D. M., Cardelli, J. A., & Sofia, U. J. 1997, *ApJ*, 490, L103
 Minter, A. H., & Spangler, S. R. 1997, *ApJ*, 485, 182
 Ogden, P. M., & Reynolds, R. J. 1985, *ApJ*, 290, 238
 Osterbrock, D. E. 1989, *Astrophysics of Gaseous Nebulae and Active Galactic Nuclei* (Mill Valley: University Science Books)
 Otte, B., & Dettmar, R.-J. 1999, *A&A*, 343, 705
 Percival, J. W. 1994, *BAAS*, 185, 6901
 ———. 1995, *Proc. SPIE*, 2479, 33
 Rand, R. J. 1998, *ApJ*, 501, 137
 ———. 1997, *ApJ*, 474, 129
 Rand, R. J., Kulkarni, S. R., & Hester, J. J. 1990, *ApJ*, 352, L1
 Reynolds, R. J. 1980, *ApJ*, 236, 153
 ———. 1985a, *ApJ*, 294, 256
 ———. 1985b, *ApJ*, 298, L27
 ———. 1988, *AJ*, 96, 670
 ———. 1997, in *The Physics of Galactic Halos*, ed. H. Lesch, R.-J. Dettmar, U. Mebold, & R. Schlickeiser (Berlin: Akademie), 57
 Reynolds, R. J., & Cox, D. P. 1992, *ApJ*, 400, L33
 Reynolds, R. J., Haffner, L. M., & Tufte, S. L. 1999, in preparation
 Reynolds, R. J., Hausen, N. R., Tufte, S. L., & Haffner, L. M. 1998a, *ApJ*, 494, L99
 Reynolds, R. J., Roesler, F. L., Scherb, F., & Harlander, J. 1990, *Proc. SPIE*, 1235, 610
 Reynolds, R. J., & Tufte, S. L. 1995, *ApJ*, 439, L17
 Reynolds, R. J., Tufte, S. L., Haffner, L. M., Jaehnig, K., & Percival, J. W. 1998b, *Publ. Astron. Soc. Australia*, 15, 14
 Reynolds, R. J., Tufte, S. L., Kung, D. T., McCullough, P. R., & Heiles, C. 1995, *ApJ*, 448, 715
 Sokolowski, J. 1994, preprint
 Tufte, S. L. 1997, Ph.D. thesis, Univ. Wisconsin–Madison
 Wang, J., Heckman, T. M., & Lehnert, M. D. 1997, *ApJ*, 491, 114